THE JOURNAL OF PHYSICAL CHEMISTRY C

Article

pubs.acs.org/JPCC

Visualization of Defect-Induced Excitonic Properties of the Edges and Grain Boundaries in Synthesized Monolayer Molybdenum Disulfide

A. E. Yore,[†] K. K. H. Smithe,[‡] W. Crumrine,[†] A. Miller,[†] J. A. Tuck,[†] B. Redd,[†] E. Pop,[‡] Bin Wang,[§] and A. K. M. Newaz*[,†]

[†]Department of Physics and Astronomy, San Francisco State University, San Francisco, California 94132, United States

[‡]Department of Electrical Engineering, Stanford University, Stanford, California 94305, United States

[§]School of Chemical, Biological and Materials Engineering, University of Oklahoma, Norman, Oklahoma 73019, United States

Supporting Information

ABSTRACT: Atomically thin two-dimensional (2D) transition-metal dichalcogenides (TMDCs) are attractive materials for next-generation nanoscale optoelectronic applications. Understanding the nanoscale optical behavior of the edges and grain boundaries of synthetically grown TMDCs is vital for optimizing their optoelectronic properties. Elucidating the nanoscale optical properties of 2D materials through far-field optical microscopy requires a diffraction-limited optical beam diameter that is submicrometer in size. Herein, we present our experimental work on the spatial photoluminescence (PL) scanning of large-size (≥50-μm) monolayer MoS_2 grown by chemical vapor deposition (CVD) using a diffraction-limited blue laser beam spot (wavelength = 405 nm) with a beam diameter as small as ∼200 nm, allowing nanoscale excitonic phenomena that had not observed before to be probed. We found several important features: (i) There exists a submicrometer-width strip (∼500 nm) along the edges that fluoresces ∼1000% brighter than the region far inside. (ii) There is another brighter wide region consisting of parallel fluorescing lines ending at the corners of the zigzag peripheral edges. (iii) There is a giant blue-shifted A excitonic peak, as large as ∼120 meV, in the PL spectra from the edges. On the basis of density functional theory calculations, we attribute this giant blue shift to the adsorption of oxygen impurities at the edges, which reduces the excitonic binding energy. Our results not only shed light on defect-induced excitonic properties but also offer an attractive route to tailoring the optical properties at TMDC edges through defect engineering.

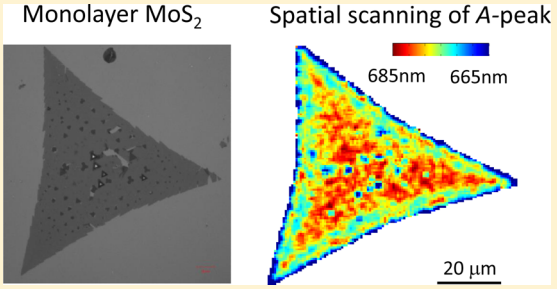

INTRODUCTION

The direct-band-gap properties of monolayer transition-metal dichalcogenides (TMDCs) provide the tantalizing prospect of miniaturizing semiconductor devices to truly atomic scales and accelerating the advances of many two-dimensional (2D) optoelectronic devices.[1] Two-dimensional confinement, the nature of the direct band gap,[2] and weak screening of charge carriers enhance the light−matter interactions[2−4] in these materials, leading to extraordinarily high absorption, creation of electron−hole (e−h) pairs, and formation of excitons (a hydrogenic entity made of an e−h pair). These extraordinary properties make TMDCs very attractive for optoelectronic applications[1,5−9] including low-power transistors,[10] sensitive photodetectors,[5,11−13] energy-harvesting devices,[14−16] atomically thin light-emitting diodes (LEDs),[6,8,9] single-photon sources,[17−21] and nanocavity lasers.[22] To realize TMDCs for practical applications, it is necessary to understand the optical properties of edges, which become dominant as devices shrink to nanoscale.[23] The edges are also important for photocatalytic, electrocatalytic, and hydrodesulfurization processes.[24]

In addition to the atomic edges, other structural defects can also have pronounced effects. Recent advances in chemical vapor deposition (CVD) have allowed for the batch production of monolayer TMDCs of macroscopic size and uniform atomic thickness.[25−28] However, these synthesized films are polycrystalline in nature largely because of the coalescence of disoriented domains,[29−31] affecting both their electrical[32,33] and optical[30] properties. It is therefore of paramount importance to understand the optical properties of the edges of these misoriented domains. So far, the far-field optical properties of TMDCs have been studied using conventional scanning microphotoluminescence (μPL) microscopy, which employs micrometer-sized or larger optical beams[34−39] and lacks sufficient resolution to probe the optical properties of the edges and the grain boundaries.

Herein, we report our study using a scanning far-field PL mapping employing an ultranarrow optical beam (∼200 nm)

Received: July 7, 2016
Revised: October 4, 2016
Published: October 5, 2016

DOI: 10.1021/acs.jpcc.6b06828
J. Phys. Chem. C 2016, 120, 24080−24087

that has allowed the observation of three important excitonic features at the atomic edges and the grain boundaries of large-size CVD-grown monolayer-MoS_2 (1L-MoS_2) flakes. First, there exists a narrow, submicrometer (width ≈ 500 nm) strip of higher fluorescence at the outermost edges of monolayer MoS_2 flakes. Second, there is a wide (∼5−10-μm) fluorescent region just inside the peripheral edge, comprising multiple parallel submicrometer fluorescent lines. Finally, the A-exciton originating from both the single-crystalline edges and the polycrystalline boundaries is significantly blue-shifted (∼120 meV) relative to the interior fluorescence. On the basis of density functional theory (DFT) calculations, we attribute the giant blue-shift phenomenon of the A-exciton to the reduced screening strength originating from the adsorption of oxygen dimers at the edges and grain boundaries. Our study not only elucidates the intricate defect-related luminescence properties of the edges but also provides a pathway, through defect engineering, for the design of the next generation of optical and optoelectronic devices.

MATERIALS AND METHODS

Sample Growth. Large flakes of 1L-MoS_2 were synthesized from solid S and MoO_3 precursors directly onto SiO_2 on Si, utilizing a seed layer of perylene-3,4,9,10-tetracarboxylic acid tetrapotassium salt (PTAS).[27,40] We utilized elevated temperature (850 °C) and atmospheric pressure to encourage epitaxial growth, which can result in single-crystal domains in excess of 200 μm on an edge (see Figure S1 in the Supporting Information). The layer thickness of the grown sample was confirmed by Raman spectroscopy[41−43] and atomic force microscopy (see Supporting Information).[27,44] A direct comparison of CVD-grown and exfoliated 1L-MoS_2 by PL and Raman spectroscopies demonstrated that the CVD-grown samples were of high quality (see Figure S2 in the Supporting Information).

Computational Methods. Density functional theory (DFT) calculations were carried out using the VASP package.[45] The Perdew−Burke−Ernzerhof (PBE) generalized gradient approximation (GGA) exchange-correlation potential[46] was used, and the electron−core interactions were treated by the projector augmented wave (PAW) method.[47,48] All calculations were performed using a MoS_2 nanoribbon with a length of 5.2 nm. The length of the supercell along the periodic direction was 1.3 nm. Structures were optimized using a single Γ-point of the Brillouin zone with a kinetic-energy cutoff of 400 eV. The structure was fully relaxed until atomic forces were smaller than 0.02 eV $Å^{-1}$. In these calculations, the spin−orbit interaction was not taken into account, because we focused on the shift of the energy bands whereas the valence-band splitting is expected to remain the same. When calculating the formation energy of oxygen impurities, we used the experimental value of gas-phase O_2 binding energy as the reference.[49]

Confocal PL Imaging. We conducted high-resolution PL scanning using a laser scanning confocal microscope (Zeiss 710 Axiovert) with an oil objective of high numerical aperture (NA = 1.4). For these experiments, we raster-scanned a focused excitation laser (λ ≈ 405 nm) over the sample and recorded PL spectra at each point. The sample was covered with a thin film of water and encapsulated by a coverslip, as shown schematically in Figure 1a. We successfully focused the beam to a spot size with a diameter of ∼200 nm; that is, the beam area was ∼25 times smaller than the micrometer-sized beam area used in the scanning PL systems conventionally used to study TMDC samples.[34−39] The beam diameter was confirmed with a calibrated fluorescent bead of diameter 200 nm (see Supporting Information), and all measurements were conducted at room temperature. The power intensity of the laser was ∼3 mW, and the dwell time at each pixel was ∼100 μs. The reflection image of a 1L-MoS_2 sample is shown in Figure 1b. The darker region on the flake originates from bilayer spots. We studied a total of 11 samples, and all demonstrated similar results (see Supporting Information). Because this high-resolution microscopy technique requires a thin aqueous layer between a coverslip and the sample, all measurements were carried out in air at room temperature.

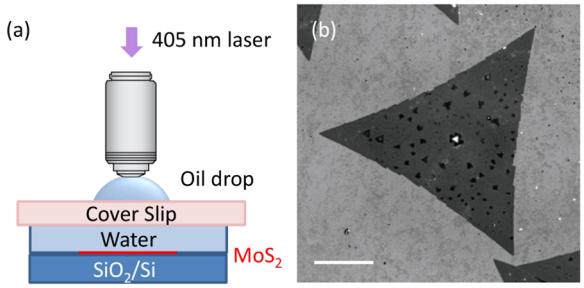

Figure 1. (a) Schematic of the experimental setup (not to scale). The sample was covered with water and encapsulated by a coverslip (thickness ≈ 0.17 mm). We used an oil objective to enhance the numerical aperture. (b) Reflection image of a 1L-MoS_2 sample. The scale bar is 20 μm. Note that the darker specks are small multilayer nucleation flakes.

RESULTS AND DISCUSSION

A high-resolution fluorescence image of a large triangular 1L-MoS_2 sample is shown in Figure 2a. In all previous studies of similar systems, the researchers have reported a wide region of fluorescence at the edges.[30,50] What is unique in our high-resolution spatial mapping is that we successfully resolved the fluorescing regions near the edges and found that the brighter edges actually consist of two distinct regions of brighter intensity.

First, our spatial mapping shows a submicrometer fluorescent strip with a width of ∼500 nm along the flake edge. The intensity profile along a line drawn across this strip is shown as an inset in Figure 2b and reveals fluorescence intensities ∼400% higher than those in the inner regions of the sample. For three samples, we observed edge fluorescence intensities ∼1000% larger than those of the interior (see Supporting Information). This extraordinarily large spike in intensity might arise from point defects, which can trap free charge carriers and localized excitons.[51] Using scanning tunneling microscopy (STM), it has been demonstrated that point defects, such as S vacancies, can form at flake edges.[52,53]

Second, our spatial PL mapping shows another wider band along the edges consisting of parallel fluorescent lines (as marked by arrows in Figure 2b). Interestingly, these parallel lines originate from the zigzag corners of the periphery, as is clearly visible in the enlarged image presented in Figure 2b. These fluorescent parallel lines have a spatial width of ∼500 nm and fluoresce with an intensity ∼100% higher than that of neighboring spots. We suggest that these fluorescent lines originate from line defects, which are boundaries between two domains with opposite rotations of the 3-fold symmetric MoS_2 lattice, as has been observed in STM measurements of physical-vapor-deposited MoS_2 on a Au(111) substrate[54] and scanning

DOI: 10.1021/acs.jpcc.6b06828
J. Phys. Chem. C 2016, 120, 24080−24087

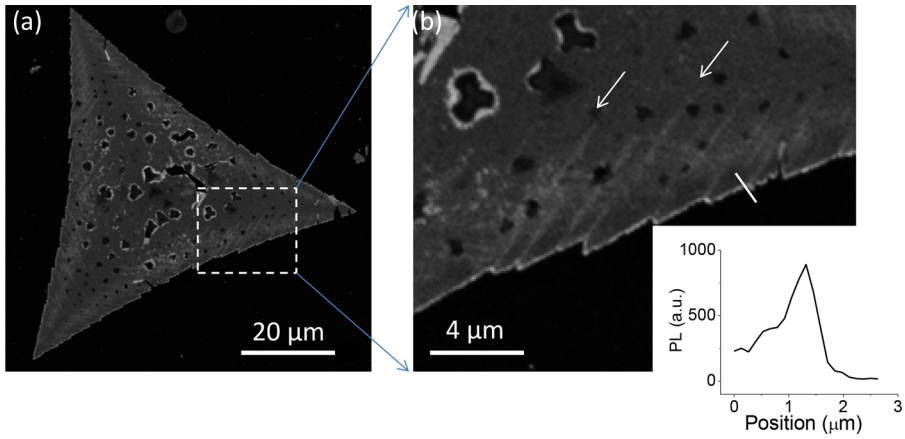

Figure 2. (a) Fluorescence image of a 1L-MoS_2 flake. (b) Enlarged view of the dashed square in panel a. The fluorescence image shows many parallel brighter lines matching the zigzag edges, as marked by white arrows. The inset shows the intensity profile along the white line drawn on the edges.

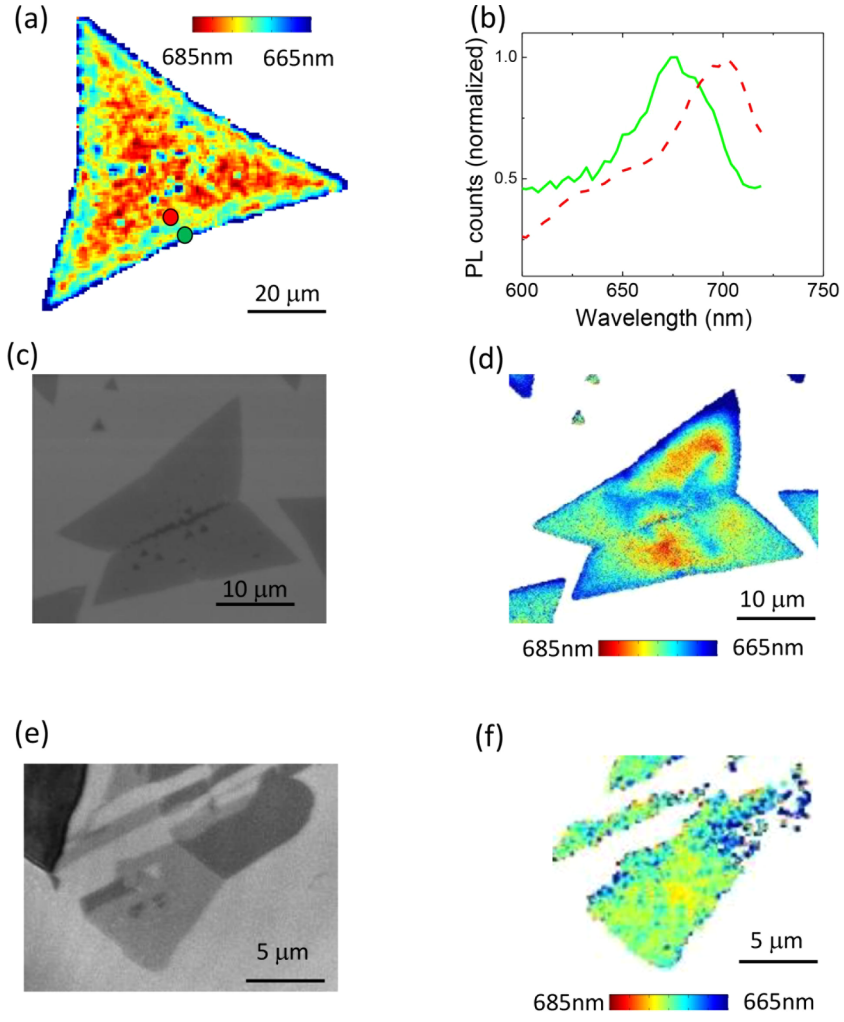

Figure 3. Spatial mapping of the A-peak position. (a) Triangular sample whose reflection image is shown in Figure 2b. (b) Photoluminescence spectra corresponding to the PL from the positions marked by green (green, solid line) and red (red, dashed line) circles in panel a. (c) Reflection image of a mirror-symmetric sample (d) Spatial mapping of the A-peak position of the mirror-symmetric sample in panel c. (e) Reflection image of an exfoliated monolayer (lightest contrast) connected to multilayer flakes. (f) Spatial mapping of the A-peak position of the microexfoliated sample shown in panel e.

transmission electron microscopy (STEM) of CVD-grown MoS_2 on SiO_2.[52] In this work, we observed the *optical* signature of these line defects for the first time. This suggests that, although the reflection image of 1L-MoS_2 shows seamless integration into a single-crystalline entity (as in Figure 1b), the flake actually consists of multiple domains, as evidenced by the fluorescing line defects along the grain boundaries. Brighter luminescence from the defects suggests that these line defects

DOI: 10.1021/acs.jpcc.6b06828
J. Phys. Chem. C 2016, 120, 24080−24087

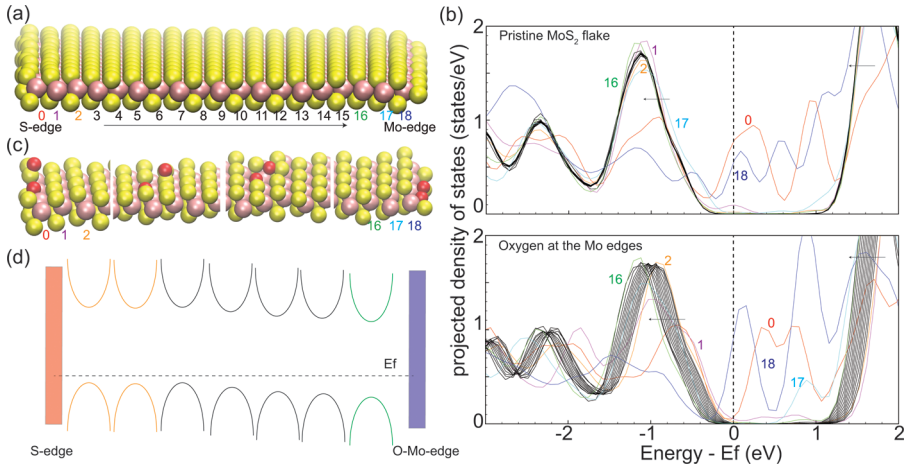

Figure 4. DFT calculations of a pristine MoS_2 nanoribbon and an oxygen-functionalized MoS_2 nanoribbon. (a) Optimized structure. (b) Projected density of states of each Mo atom indexed in panel a. (c) Different configurations of oxygen dimers at various locations in the nanoribbon. (d) Schematics showing enhanced n-type doping caused by oxygen dimers at the Mo edge. The metallic edges are indicated by the continuous states.

might trap excitons and behave similarly to the point defects at the periphery.

To understand the origin of the brighter edges, we further investigated wavelength-resolved PL scans of our 1L-MoS_2 samples. After pumping the flakes with a ~405-nm laser, we observed a major luminescence peak shift across the sample, ranging from 660 nm at the edge to 710 nm farther inward. This peak in PL, also known as an A-exciton peak (A-peak), has been attributed to the recombination of photoexcited excitons across the direct band gap at the K-point.[2,4] The spatial mapping of the wavelength values of the A-peak for that same large triangular flake and another polycrystalline sample are shown in panels a and c,d, respectively, of Figure 3. Figure 3b shows the PL spectra of two locations in the sample shown in Figure 3a, one at the periphery and the other just inside. Here, the peak positions were obtained by fitting the PL data for every pixel using a Gaussian profile. For the pixels for which Gaussian fitting was not possible (i.e., for the pixels outside the flake), the color was set to white. A very strong blue-shifted A-peak was observed at the flake edges relative to interior. The maximum energy of the edge A-peak was ~1.89 eV (~656 nm), and the minimum energy of the interior A-peak was 1.77 eV (~703 nm). This represents a total upshift of ~120 meV, approximately ~3 times larger than previously reported values.[50] We did not observe any dependence of the PL blue shift or intensity on the flake size (see Figure S6).

To investigate the effect of the beam diameter on the PL mapping, we varied the laser beam size. We observed that the upshift values decreased significantly when we employed wider beam spots; specifically, the blue shift decreased to ~20 meV when we doubled the beam diameter (from 200 to 400 nm). For a beam with a size of a few micrometers, there was no observable blue shift. These findings are expected, as wider beams include PL signals from areas farther into the flake's interior, averaging out the A-peak and minimizing the blue shift.

We now discuss possible origins of our observations of giant blue shifts of A-exciton peaks. Various studies have shown that large shifts of the A-exciton peak can originate from edge stress or compression,[55−58] neutral exction−trion population,[50] spatial confinement,[59] and defects.[60−62] Specifically, it has been experimentally demonstrated that compressive strain can lead to a blue shift in the A-exciton peak;[58] and furthermore, DFT calculations have predicted that the edges of MoS_2 flakes are, in fact, naturally compressed relative to the interior.[63] Hence, the presence of compressive strain at the edges can cause a blue shift in the A-peak. The Raman spectrum from the edges demonstrates a slight compressive strain (~0.1%) that will cause a blue shift of the A-exciton by only ~5 meV (see Figure S4 in the Supporting Information).[64] Furthermore, to examine the effects of edge strain on the observed optical properties, we also studied the spatial scanning of PL for several 1L-MoS_2 samples prepared by microexfoliation and did not observe any blue-shifted edges, as shown in Figure 3e,f. We examined more than five microexfoliated 1L-MoS_2 samples and observed similar results. Thus, we argue that the observed giant blue shift of the A-peak cannot be due to compressive strain at the edges. The observed giant blue shift of the A-exciton might also arise from the competition between trion and neutral exciton population. Because we observed a blue shift much larger than the binding energy (~20 meV) of the trions, we can safely rule out the possibility that the observed giant blue shift originates from the relative competition between trion and neutral exciton population.

It has been demonstrated that spatial confinement reduces the screening strength and increases the Coulomb interaction and exciton binding energy.[59,65] Hence, it is expected that spatial confinement at the edges of 1L-MoS_2 samples would modify the exciton binding energy and luminescing photon energy. The width of region for which the A-peak has been blue-shifted, however, is ~500 nm, which is very large compared to the physical size of the excitons (~1−3 nm).[53] Moreover, we did not observe any blue shift for the A-exciton in the microexfoliated samples, where excitons would encounter similar edge confinement. Thus, it is unlikely that the large blue shift originates from the spatial confinement at the edge.

Now, we concentrate on edge defects and how they can modify the PL A-peak and the fluorescence intensity. Edge defects were explored using first-principles DFT calculations (see details in the Computational Methods section). To model the flakes used in the experiments, we used a nanoribbon that was periodic in one direction and had a finite width in the other. All calculations were performed using a MoS_2 nanoribbon with a width of 5.2 nm. The width was sufficient to eliminate the effects of the edges on the middle of the ribbon, as shown by the converged density of states (DOS) when

DOI: 10.1021/acs.jpcc.6b06828
J. Phys. Chem. C 2016, 120, 24080−24087

moving from the edge toward the middle in Figure 4b (top panel).

The MoS_2 nanoribbons used in our calculations are shown in Figure 4a,c. The ribbon was terminated by two edges, the S edge and the Mo edge. Previous studies of MoS_2 nanocrystals using atomic-resolution STM have shown that both edges can be present.[53,66,67] The Mo edge exhibits a specific metallic electronic structure and has been shown to dominate in triangular MoS_2 nanocrystals supported on the Au(111) surface.[68] The Mo edge has been shown to be the key active site for both the hydrogen evolution reaction[69] and the hydrodesulfurization reaction.[70] Figure 4b (top panel) shows the projected density of states (PDOS) of each Mo atom across the nanoribbons because the 4d states of the Mo atoms dominate the band edge states. The two edges show some metallic character, in agreement with a previous STM study.[68] When moving toward the middle of the ribbon, there is less difference between the Mo atoms, all of which converge to the bulk electronic structure.

It has been shown experimentally that S vacancies form at the edges[52,53] and can be saturated by oxygen during the fabrication process used in this work. The oxidation of the edges was also reported experimentally in STM measurements of air-exposed monolayer WSe_2.[71] X-ray photoelectron spectroscopy data from a thick MoS_2 sample suggested that oxygen molecules can be adsorbed at the cracks and vacancies.[61] Previous calculations suggested that local strain at the grain boundaries in monolayer materials can also attract and accumulate oxygen.[72] Here, we studied oxygen dimer, which forms by dissociation of an oxygen molecule at a sulfur vacancy. It is more energetically favorable by 0.6 eV at the Mo edge and by 0.4 eV at the S edge as compared to the middle of the ribbon (Figure 4c), which indicates a inhomogeneous distribution of oxygen dimers. Figure 4b (bottom panel) shows plots of the PDOS of each Mo atom when an oxygen dimer is located at the Mo edge (the most stable configuration). A more pronounced electronic resonance from the edge atom (index $n = 18$) is caused by the oxygen dimer, which introduces more valence electrons than the replaced S atom that previously occupied the position. In addition, there is a gradual downshift of the valence band with respect to the Fermi level when moving toward the Mo edge, as schematically shown in Figure 4d. This downshift of the valence bands is caused by a surface dipole resulting from the oxygen-induced charge redistribution, which is also shown by the change in the local electrostatic potential plotted 3.5 Å above the MoS_2 surface (see Figure S8 in the Supporting Information). The change in the local electrostatic potential remains the same when the vacuum layer is increased further to 5 nm (see Figure S9). The correlation between the increased electron density suggested by the calculations, which is mainly localized at the edge of the ribbon, and the blue shift of the PL at the edges found experimentally suggests that enhanced screening of the excited electron from its counterpart—the remaining hole in the valence band—can lead to a reduced exciton binding energy and provides an explanation for the blue shift of the PL peak at the edges. The long-range screening effect extends to a distance of about 500 nm, as shown by the blue-shifted A-peak. However, the ground-state DFT calculations cannot resolve the dependence of the screening effect on the distance from the metallic edge.

We found that an oxygen monomer, instead of an oxygen dimer, at the S vacancy causes similar changes in the electronic structure (Figure S10). The calculated energy gain to incorporate an oxygen atom at a sulfur vacancy at the Mo edge is 4.8 eV, whereas the energy gain for an oxygen dimer is 4.5 eV per O atom. We found that substitutional oxygen exhibits little variation in formation energy across the ribbon; however, preference for the formation of a sulfur vacancy at the edges might drive the inhomogeneous distribution of sulfur vacancies and also substitutional oxygen monomers. The similar energy gains for the incorporations of oxygen monomer and dimer suggest that oxygen might exist as dimers at low concentrations of sulfur vacancies whereas oxygen monomer dominates at high concentrations of sulfur vacancies because of the diffusion of oxygen atoms.

Intriguingly, our findings using a far-field optical microscope involving an ultranarrow beam were very different from the results reported recently by Bao et al.[50] using a ∼60-nm-diameter beam in a near-field scanning optical microscope setup. First, we observed a larger (∼2.5 times) blue shift of the A-excitons at the periphery. Second, we observed exciton-enhancing luminescence at the periphery in agreement with other studies,[30] whereas Bao et al. observed exciton-quenching luminescence. Although currently not understood, the discrepancies might be attributable to different sample growth procedures and different sizes of the samples (our samples were at least one order of magnitude larger), both of which can affect the defect concentration and, in turn, the PL measurement.

CONCLUSIONS

In summary, we performed the ultra-high-resolution fluorescence imaging and spatial mapping of 1L-MoS_2 using a narrow optical beam and found several important characteristics at the edges. We observed a strip of brighter fluorescence at the outermost edge and another wide region of brighter luminescence consisting of submicrometer parallel lines originating from sharp zigzag corners due to line defects. The latter suggests that large flakes are, in fact, polycrystalline at the edges. Moreover, we observed a giant blue-shifted A-exciton peak at the edges. On the basis of DFT calculations, we attribute this blue shift to the adsorption of oxygen impurities at the edges, which reduces the binding energy of the exciton, resulting in a blue-shifted A-exciton peak. Our results are important for informing the design of next-generation truly nanoscale or atomic-scale optical and optoelectronic devices, because edge effects become dominant as devices reduce in size to the nanoscale.

ASSOCIATED CONTENT

Supporting Information

The Supporting Information is available free of charge on the ACS Publications website at DOI: 10.1021/acs.jpcc.6b06828.

Results from other samples, AFM images, Raman data, PL data, optical-beam-diameter measurement, data on exfoliated samples, and supporting DFT calculations (PDF)

AUTHOR INFORMATION

Corresponding Author

*E-mail: akmnewaz@sfsu.edu. Phone: 415-338-2944.

Notes

The authors declare no competing financial interest.

DOI: 10.1021/acs.jpcc.6b06828
J. Phys. Chem. C 2016, 120, 24080−24087

■ ACKNOWLEDGMENTS

We thank Dr. Annette Chan for the help in performing the spatial PL scanning. A.K.M.N. and A.E.Y. are grateful for the financial support from SFSU. K.K.H.S. and E.P. acknowledge support from AFOSR Grant FA9550-14-1-0251 and NSF EFRI 2-DARE Grant 1542883. K.K.H.S. also acknowledges partial support from the Stanford Graduate Fellowship program and an NSF Graduate Research Fellowship under Grant DGE-114747. This research used the Cell and Molecular Imaging Center at SFSU. This research also used computational resources of the National Energy Research Scientific Computing Center (NERSC), a U.S. Department of Energy (DOE) Office of Science User Facility supported by the Office of Science of the U.S. DOE.

■ REFERENCES

(1) Wang, Q. H.; Kalantar-Zadeh, K.; Kis, A.; Coleman, J. N.; Strano, M. S. Electronics and Optoelectronics of Two-Dimensional Transition Metal Dichalcogenides. *Nat. Nanotechnol.* **2012**, *7*, 699−712.

(2) Mak, K. F.; Lee, C.; Hone, J.; Shan, J.; Heinz, T. F. Atomically Thin MoS_2: A New Direct-Gap Semiconductor. *Phys. Rev. Lett.* **2010**, *105*, 136805.

(3) Britnell, L.; Ribeiro, R. M.; Eckmann, A.; Jalil, R.; Belle, B. D.; Mishchenko, A.; Kim, Y.-J.; Gorbachev, R. V.; Georgiou, T.; Morozov, S. V.; et al. Strong Light-Matter Interactions in Heterostructures of Atomically Thin Films. *Science* **2013**, *340*, 1311−1314.

(4) Splendiani, A.; Sun, L.; Zhang, Y.; Li, T.; Kim, J.; Chim, C.-Y.; Galli, G.; Wang, F. Emerging Photoluminescence in Monolayer MoS_2. *Nano Lett.* **2010**, *10*, 1271−1275.

(5) Lopez-Sanchez, O.; Lembke, D.; Kayci, M.; Radenovic, A.; Kis, A. Ultrasensitive Photodetectors Based on Monolayer MoS_2. *Nat. Nanotechnol.* **2013**, *8*, 497−501.

(6) Baugher, B. W. H.; Churchill, H. O. H.; Yang, Y.; Jarillo-Herrero, P. Optoelectronic Devices Based on Electrically Tunable P-N Diodes in a Monolayer Dichalcogenide. *Nat. Nanotechnol.* **2014**, *9*, 262−267.

(7) Eda, G.; Maier, S. A. Two-Dimensional Crystals: Managing Light for Optoelectronics. *ACS Nano* **2013**, *7*, 5660−5665.

(8) Ross, J. S.; Klement, P.; Jones, A. M.; Ghimire, N. J.; Yan, J.; Mandrus, D. G.; Taniguchi, T.; Watanabe, K.; Kitamura, K.; Yao, W.; et al. Electrically Tunable Excitonic Light-Emitting Diodes Based on Monolayer WSe_2 P-N Junctions. *Nat. Nanotechnol.* **2014**, *9*, 268−272.

(9) Sundaram, R. S.; Engel, M.; Lombardo, A.; Krupke, R.; Ferrari, A. C.; Avouris, P.; Steiner, M. Electroluminescence in Single Layer MoS_2. *Nano Lett.* **2013**, *13*, 1416−1421.

(10) Wang, H.; Yu, L.; Lee, Y.-H.; Fang, W.; Hsu, A.; Herring, P.; Chin, M.; Dubey, M.; Li, L.-J.; Kong, J.; Palacios, T. Large-Scale 2D Electronics Based on Single-Layer MoS_2 Grown by Chemical Vapor Deposition. In *2012 International Electron Devices Meeting: Technical Digest*; IEEE Press: Piscataway, NJ, 2012; pp 4.6.1−4.6.4 (accessed August 3, 2016).

(11) Tsai, D.-S.; Liu, K.-K.; Lien, D.-H.; Tsai, M.-L.; Kang, C.-F.; Lin, C.-A.; Li, L.-J.; He, J.-H. Few-Layer MoS_2 with High Broadband Photogain and Fast Optical Switching for Use in Harsh Environments. *ACS Nano* **2013**, *7*, 3905−3911.

(12) Wu, C.-C.; Jariwala, D.; Sangwan, V. K.; Marks, T. J.; Hersam, M. C.; Lauhon, L. J. Elucidating the Photoresponse of Ultrathin MoS_2 Field-Effect Transistors by Scanning Photocurrent Microscopy. *J. Phys. Chem. Lett.* **2013**, *4*, 2508−2513.

(13) Yin, Z.; Li, H.; Li, H.; Jiang, L.; Shi, Y.; Sun, Y.; Lu, G.; Zhang, Q.; Chen, X.; Zhang, H. Single-Layer MoS_2 Phototransistors. *ACS Nano* **2012**, *6*, 74−80.

(14) Tsai, M.-L.; Su, S.-H.; Chang, J.-K.; Tsai, D.-S.; Chen, C.-H.; Wu, C.-I.; Li, L.-J.; Chen, L.-J.; He, J.-H. Monolayer MoS_2 Heterojunction Solar Cells. *ACS Nano* **2014**, *8*, 8317−8322.

(15) Bernardi, M.; Palummo, M.; Grossman, J. C. Extraordinary Sunlight Absorption and One Nanometer Thick Photovoltaics Using Two-Dimensional Monolayer Materials. *Nano Lett.* **2013**, *13*, 3664−3670.

(16) Peng, B.; Ang, P. K.; Loh, K. P. Two-Dimensional Dichalcogenides for Light-Harvesting Applications. *Nano Today* **2015**, *10*, 128−137.

(17) Tonndorf, P.; Schmidt, R.; Schneider, R.; Kern, J.; Buscema, M.; Steele, G. A.; Castellanos-Gomez, A.; van der Zant, H. S. J.; Michaelis de Vasconcellos, S.; Bratschitsch, R. Single-Photon Emission from Localized Excitons in an Atomically Thin Semiconductor. *Optica* **2015**, *2*, 347−352.

(18) Chakraborty, C.; Kinnischtzke, L.; Goodfellow, K. M.; Beams, R.; Vamivakas, A. N. Voltage-Controlled Quantum Light from an Atomically Thin Semiconductor. *Nat. Nanotechnol.* **2015**, *10*, 507−511.

(19) He, Y.-M.; Clark, G.; Schaibley, J. R.; He, Y.; Chen, M.-C.; Wei, Y.-J.; Ding, X.; Zhang, Q.; Yao, W.; Xu, X.; et al. Single Quantum Emitters in Monolayer Semiconductors. *Nat. Nanotechnol.* **2015**, *10*, 497−502.

(20) Srivastava, A.; Sidler, M.; Allain, A. V.; Lembke, D. S.; Kis, A.; Imamoğlu, A. Optically Active Quantum Dots in Monolayer WSe_2. *Nat. Nanotechnol.* **2015**, *10*, 491−496.

(21) Koperski, M.; Nogajewski, K.; Arora, A.; Cherkez, V.; Mallet, P.; Veuillen, J. Y.; Marcus, J.; Kossacki, P.; Potemski, M. Single Photon Emitters in Exfoliated WSe_2 Structures. *Nat. Nanotechnol.* **2015**, *10*, 503−506.

(22) Wu, S.; Buckley, S.; Schaibley, J. R.; Feng, L.; Yan, J.; Mandrus, D. G.; Hatami, F.; Yao, W.; Vučković, J.; Majumdar, A.; Xu, X. Monolayer semiconductor nanocavity lasers with ultralow thresholds. *Nature* **2015**, *520*, 69−72.

(23) Chang, S.-L.; Lin, S.-Y.; Lin, S.-K.; Lee, C.-H.; Lin, M.-F. Geometric and Electronic Properties of Edge-Decorated Graphene Nanoribbons. *Sci. Rep.* **2014**, *4*, 6038.

(24) Kibsgaard, J.; Chen, Z.; Reinecke, B. N.; Jaramillo, T. F. Engineering the Surface Structure of MoS_2 To Preferentially Expose Active Edge Sites for Electrocatalysis. *Nat. Mater.* **2012**, *11*, 963−969.

(25) Huang, J.-K.; Pu, J.; Hsu, C.-L.; Chiu, M.-H.; Juang, Z.-Y.; Chang, Y.-H.; Chang, W.-H.; Iwasa, Y.; Takenobu, T.; Li, L.-J. Large-Area Synthesis of Highly Crystalline WSe_2 Monolayers and Device Applications. *ACS Nano* **2014**, *8*, 923−930.

(26) Liu, K.-K.; Zhang, W.; Lee, Y.-H.; Lin, Y.-C.; Chang, M.-T.; Su, C.-Y.; Chang, C.-S.; Li, H.; Shi, Y.; Zhang, H.; et al. Growth of Large-Area and Highly Crystalline MoS_2 Thin Layers on Insulating Substrates. *Nano Lett.* **2012**, *12*, 1538−1544.

(27) Lee, Y.-H.; Zhang, X.-Q.; Zhang, W.; Chang, M.-T.; Lin, C.-T.; Chang, K.-D.; Yu, Y.-C.; Wang, J. T.-W.; Chang, C.-S.; Li, L.-J.; et al. Synthesis of Large-Area MoS_2 Atomic Layers with Chemical Vapor Deposition. *Adv. Mater.* **2012**, *24*, 2320−2325.

(28) Zhan, Y.; Liu, Z.; Najmaei, S.; Ajayan, P. M.; Lou, J. Large-Area Vapor-Phase Growth and Characterization of MoS_2 Atomic Layers on a SiO_2 Substrate. *Small* **2012**, *8*, 966−971.

(29) Ji, Q.; Kan, M.; Zhang, Y.; Guo, Y.; Ma, D.; Shi, J.; Sun, Q.; Chen, Q.; Zhang, Y.; Liu, Z. Unravelling Orientation Distribution and Merging Behavior of Monolayer MoS_2 Domains on Sapphire. *Nano Lett.* **2015**, *15*, 198−205.

(30) van der Zande, A. M.; Huang, P. Y.; Chenet, D. A.; Berkelbach, T. C.; You, Y.; Lee, G.-H.; Heinz, T. F.; Reichman, D. R.; Muller, D. A.; Hone, J. C. Grains and Grain Boundaries in Highly Crystalline Monolayer Molybdenum Disulphide. *Nat. Mater.* **2013**, *12*, 554−561.

(31) Huang, P. Y.; Ruiz-Vargas, C. S.; van der Zande, A. M.; Whitney, W. S.; Levendorf, M. P.; Kevek, J. W.; Garg, S.; Alden, J. S.; Hustedt, C. J.; Zhu, Y.; et al. Grains and Grain Boundaries in Single-Layer Graphene Atomic Patchwork Quilts. *Nature* **2011**, *469*, 389−392.

(32) Azcatl, A.; McDonnell, S.; K. C., S.; Peng, X.; Dong, H.; Qin, X.; Addou, R.; Mordi, G. I.; Lu, N.; Kim, J.; et al. MoS_2 Functionalization for Ultra-Thin Atomic Layer Deposited Dielectrics. *Appl. Phys. Lett.* **2014**, *104*, 111601.

(33) Ly, T. H.; Perello, D. J.; Zhao, J.; Deng, Q.; Kim, H.; Han, G. H.; Chae, S. H.; Jeong, H. Y.; Lee, Y. H. Misorientation-Angle-

DOI: 10.1021/acs.jpcc.6b06828
J. Phys. Chem. C 2016, 120, 24080−24087

Dependent Electrical Transport across Molybdenum Disulfide Grain Boundaries. *Nat. Commun.* **2016**, *7*, 10426.
(34) Kim, J. G.; Yun, W. S.; Jo, S.; Lee, J.; Cho, C. H. Effect of Interlayer Interactions on Exciton Luminescence in Atomic-Layered MoS_2 Crystals. *Sci. Rep.* **2016**, *6*, 29813.
(35) Wang, Z.; Dong, Z.; Gu, Y.; Chang, Y.-H.; Zhang, L.; Li, L.-J.; Zhao, W.; Eda, G.; Zhang, W.; Grinblat, G.; et al. Giant Photoluminescence Enhancement in Tungsten−Diselenide−Gold Plasmonic Hybrid Structures. *Nat. Commun.* **2016**, *7*, 11283.
(36) Oh, H. M.; Han, G. H.; Kim, H.; Bae, J. J.; Jeong, M. S.; Lee, Y. H. Photochemical Reaction in Monolayer MoS_2 via Correlated Photoluminescence, Raman Spectroscopy, and Atomic Force Microscopy. *ACS Nano* **2016**, *10*, 5230−5236.
(37) Mann, J.; Sun, D.; Ma, Q.; Chen, J.-R.; Preciado, E.; Ohta, T.; Diaconescu, B.; Yamaguchi, K.; Tran, T.; Wurch, M.; et al. Facile Growth of Monolayer MoS_2 Film Areas on SiO_2. *Eur. Phys. J. B* **2013**, *86*, 226.
(38) Hong, X.; Kim, J.; Shi, S.-F.; Zhang, Y.; Jin, C.; Sun, Y.; Tongay, S.; Wu, J.; Zhang, Y.; Wang, F. Ultrafast Charge Transfer in Atomically Thin MoS_2/WS_2 Heterostructures. *Nat. Nanotechnol.* **2014**, *9*, 682−686.
(39) Lezama, I. G.; Arora, A.; Ubaldini, A.; Barreteau, C.; Giannini, E.; Potemski, M.; Morpurgo, A. F. Indirect-to-Direct Band Gap Crossover in Few-Layer $MoTe_2$. *Nano Lett.* **2015**, *15*, 2336−2342.
(40) Smithe, K. K. H., English, C. D.; Suryavanshi, S. V.; Pop, E. Enhanced Electrical Transport and Performance Projections of Synthetic Monolayer MoS_2 Devices. 2016, arXiv:1608.00987. arXiv.org e-Print archive. https://arxiv.org/abs/1608.00987.
(41) Li, H.; Zhang, Q.; Yap, C. C. R.; Tay, B. K.; Edwin, T. H. T.; Olivier, A.; Baillargeat, D. From Bulk to Monolayer MoS_2: Evolution of Raman Scattering. *Adv. Funct. Mater.* **2012**, *22*, 1385−1390.
(42) Zhang, X.; Qiao, X.-F.; Shi, W.; Wu, J.-B.; Jiang, D.-S.; Tan, P.-H. Phonon and Raman Scattering of Two-Dimensional Transition Metal Dichalcogenides from Monolayer, Multilayer to Bulk Material. *Chem. Soc. Rev.* **2015**, *44*, 2757−2785.
(43) Lee, C.; Yan, H.; Brus, L. E.; Heinz, T. F.; Hone, J.; Ryu, S. Anomalous Lattice Vibrations of Single- and Few-Layer MoS_2. *ACS Nano* **2010**, *4*, 2695−2700.
(44) Radisavljevic, B.; Radenovic, A.; Brivio, J.; Giacometti, V.; Kis, A. Single-Layer MoS_2 Transistors. *Nat. Nanotechnol.* **2011**, *6*, 147−150.
(45) Kresse, G.; Furthmuller, J. Efficient Iterative Schemes for Ab Initio Total-Energy Calculations Using a Plane-Wave Basis Set. *Phys. Rev. B: Condens. Matter Mater. Phys.* **1996**, *54*, 11169−11186.
(46) Perdew, J. P.; Burke, K.; Ernzerhof, M. Generalized Gradient Approximation Made Simple. *Phys. Rev. Lett.* **1996**, *77*, 3865−3868.
(47) Blochl, P. E. Projector Augmented-Wave Method. *Phys. Rev. B: Condens. Matter Mater. Phys.* **1994**, *50*, 17953−17979.
(48) Kresse, G.; Joubert, D. From Ultrasoft Pseudopotentials to the Projector Augmented-Wave Method. *Phys. Rev. B: Condens. Matter Mater. Phys.* **1999**, *59*, 1758−1775.
(49) Herzberg, G.; Huber, K. P. *Molecular Spectra and Molecular Structure. IV. Constants of Diatomic Molecules*; Van Nostrand Reinhold Company: New York, 1979.
(50) Bao, W.; Borys, N. J.; Ko, C.; Suh, J.; Fan, W.; Thron, A.; Zhang, Y.; Buyanin, A.; Zhang, J.; Cabrini, S.; et al. Visualizing Nanoscale Excitonic Relaxation Properties of Disordered Edges and Grain Boundaries in Monolayer Molybdenum Disulfide. *Nat. Commun.* **2015**, *6*, 7993.
(51) Yin, J.; Li, X. M.; Yu, J.; Zhang, Z. H.; Zhou, J. X.; Guo, W. L. Generating Electricity by Moving a Droplet of Ionic Liquid Along Graphene. *Nat. Nanotechnol.* **2014**, *9*, 378−383.
(52) Zhou, W.; Zou, X.; Najmaei, S.; Liu, Z.; Shi, Y.; Kong, J.; Lou, J.; Ajayan, P. M.; Yakobson, B. I.; Idrobo, J.-C. Intrinsic Structural Defects in Monolayer Molybdenum Disulfide. *Nano Lett.* **2013**, *13*, 2615−2622.
(53) Helveg, S.; Lauritsen, J. V.; Lægsgaard, E.; Stensgaard, I.; Nørskov, J. K.; Clausen, B. S.; Topsøe, H.; Besenbacher, F. Atomic-Scale Structure of Single-Layer MoS_2 Nanoclusters. *Phys. Rev. Lett.* **2000**, *84*, 951−954.
(54) Grønborg, S. S.; Ulstrup, S.; Bianchi, M.; Dendzik, M.; Sanders, C. E.; Lauritsen, J. V.; Hofmann, P.; Miwa, J. A. Synthesis of Epitaxial Single-Layer MoS_2 on Au(111). *Langmuir* **2015**, *31*, 9700−9706.
(55) Conley, H. J.; Wang, B.; Ziegler, J. I.; Haglund, R. F.; Pantelides, S. T.; Bolotin, K. I. Bandgap Engineering of Strained Monolayer and Bilayer MoS_2. *Nano Lett.* **2013**, *13*, 3626−3630.
(56) Liu, Z.; Amani, M.; Najmaei, S.; Xu, Q.; Zou, X.; Zhou, W.; Yu, T.; Qiu, C.; Birdwell, A. G.; Crowne, F. J.; et al. Strain and Structure Heterogeneity in MoS_2 Atomic Layers Grown by Chemical Vapour Deposition. *Nat. Commun.* **2014**, *5*, 5246.
(57) Lu, Q.; Huang, R. Excess Energy and Deformation Along Free Edges of Graphene Nanoribbons. *Phys. Rev. B: Condens. Matter Mater. Phys.* **2010**, *81*, 155410.
(58) Hui, Y. Y.; Liu, X.; Jie, W.; Chan, N. Y.; Hao, J.; Hsu, Y.-T.; Li, L.-J.; Guo, W.; Lau, S. P. Exceptional Tunability of Band Energy in a Compressively Strained Trilayer MoS_2 Sheet. *ACS Nano* **2013**, *7*, 7126−7131.
(59) Zhu, B.; Chen, X.; Cui, X. Exciton Binding Energy of Monolayer WS_2. *Sci. Rep.* **2015**, *5*, 9218.
(60) Tongay, S.; Suh, J.; Ataca, C.; Fan, W.; Luce, A.; Kang, J. S.; Liu, J.; Ko, C.; Raghunathanan, R.; Zhou, J.; et al. Defects Activated Photoluminescence in Two-Dimensional Semiconductors: Interplay between Bound, Charged, and Free Excitons. *Sci. Rep.* **2013**, *3*, 2657.
(61) Nan, H.; Wang, Z.; Wang, W.; Liang, Z.; Lu, Y.; Chen, Q.; He, D.; Tan, P.; Miao, F.; Wang, X.; et al. Strong Photoluminescence Enhancement of MoS_2 through Defect Engineering and Oxygen Bonding. *ACS Nano* **2014**, *8*, 5738−5745.
(62) Chow, P. K.; Jacobs-Gedrim, R. B.; Gao, J.; Lu, T.-M.; Yu, B.; Terrones, H.; Koratkar, N. Defect-Induced Photoluminescence in Monolayer Semiconducting Transition Metal Dichalcogenides. *ACS Nano* **2015**, *9*, 1520−1527.
(63) Qi, Z.; Cao, P.; Park, H. S. Density Functional Theory Calculation of Edge Stresses in Monolayer MoS_2. *J. Appl. Phys.* **2013**, *114*, 163508.
(64) Rice, C.; Young, R. J.; Zan, R.; Bangert, U.; Wolverson, D.; Georgiou, T.; Jalil, R.; Novoselov, K. S. Raman-Scattering Measurements and First-Principles Calculations of Strain-Induced Phonon Shifts in Monolayer MoS_2. *Phys. Rev. B: Condens. Matter Mater. Phys.* **2013**, *87*, 081307.
(65) Klots, A. R.; Newaz, A. K. M.; Wang, B.; Prasai, D.; Krzyzanowska, H.; Lin, J.; Caudel, D.; Ghimire, N. J.; Yan, J.; Ivanov, B. L.; et al. Probing Excitonic States in Suspended Two-Dimensional Semiconductors by Photocurrent Spectroscopy. *Sci. Rep.* **2014**, *4*, 6608.
(66) Besenbacher, F.; Brorson, M.; Clausen, B. S.; Helveg, S.; Hinnemann, B.; Kibsgaard, J.; Lauritsen, J. V.; Moses, P. G.; Nørskov, J. K.; Topsøe, H. Recent Stm, Dft and Haadf-Stem Studies of Sulfide-Based Hydrotreating Catalysts: Insight into Mechanistic, Structural and Particle Size Effects. *Catal. Today* **2008**, *130*, 86−96.
(67) Lauritsen, J. V.; Kibsgaard, J.; Helveg, S.; Topsøe, H.; Clausen, B. S.; Laegsgaard, E.; Besenbacher, F. Size-Dependent Structure of MoS_2 Nanocrystals. *Nat. Nanotechnol.* **2007**, *2*, 53−58.
(68) Bollinger, M. V.; Lauritsen, J. V.; Jacobsen, K. W.; Nørskov, J. K.; Helveg, S.; Besenbacher, F. One-Dimensional Metallic Edge States in MoS_2. *Phys. Rev. Lett.* **2001**, *87*, 196803.
(69) Hinnemann, B.; Moses, P. G.; Bonde, J.; Jørgensen, K. P.; Nielsen, J. H.; Horch, S.; Chorkendorff, I.; Nørskov, J. K. Biomimetic Hydrogen Evolution: MoS_2 Nanoparticles as Catalyst for Hydrogen Evolution. *J. Am. Chem. Soc.* **2005**, *127*, 5308−5309.
(70) Moses, P. G.; Hinnemann, B.; Topsøe, H.; Nørskov, J. K. The Hydrogenation and Direct Desulfurization Reaction Pathway in Thiophene Hydrodesulfurization over MoS_2 Catalysts at Realistic Conditions: A Density Functional Study. *J. Catal.* **2007**, *248*, 188−203.
(71) Park, J. H.; Vishwanath, S.; Liu, X.; Zhou, H.; Eichfeld, S. M.; Fullerton-Shirey, S. K.; Robinson, J. A.; Feenstra, R. M.; Furdyna, J.; Jena, D.; et al. Scanning Tunneling Microscopy and Spectroscopy of Air Exposure Effects on Molecular Beam Epitaxy Grown WSe_2Monolayers and Bilayers. *ACS Nano* **2016**, *10*, 4258−4267.

DOI: 10.1021/acs.jpcc.6b06828
J. Phys. Chem. C 2016, 120, 24080−24087

(72) Wang, B.; Puzyrev, Y. S.; Pantelides, S. T. Enhanced Chemical Reactions of Oxygen at Grain Boundaries in Polycrystalline Graphene. *Polyhedron* **2013**, *64*, 158−162.

DOI: 10.1021/acs.jpcc.6b06828
J. Phys. Chem. C 2016, 120, 24080−24087

Supplementary Information

Visualization of Defect-Induced Excitonic Properties of the Edges and Grain Boundaries in Synthesized Monolayer Molybdenum Disulfide

A. E. Yore[⊥], K.K.H. Smithe[¶], W. Crumrine[⊥], A. Miller[⊥], J. A. Tuck[⊥], B. Redd[⊥], E. Pop[¶], Bin Wang[§], A.K.M. Newaz[⊥]

[⊥]Department of Physics and Astronomy, San Francisco State University, San Francisco, CA-94132, USA

[¶]Department of Electrical Engineering, Stanford University, Stanford, CA 94305, USA

[§]School of Chemical, Biological and Materials Engineering, University of Oklahoma, Norman, OK 73019, USA

S1: Optical image of CVD grown 1L-MoS_2

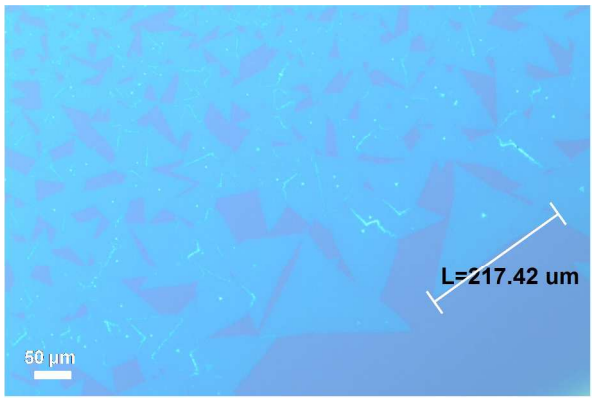

Figure S1: The optical image of CVD grown 1L-MoS2.

S2: Raman and AFM characterization of 1L-MoS_2

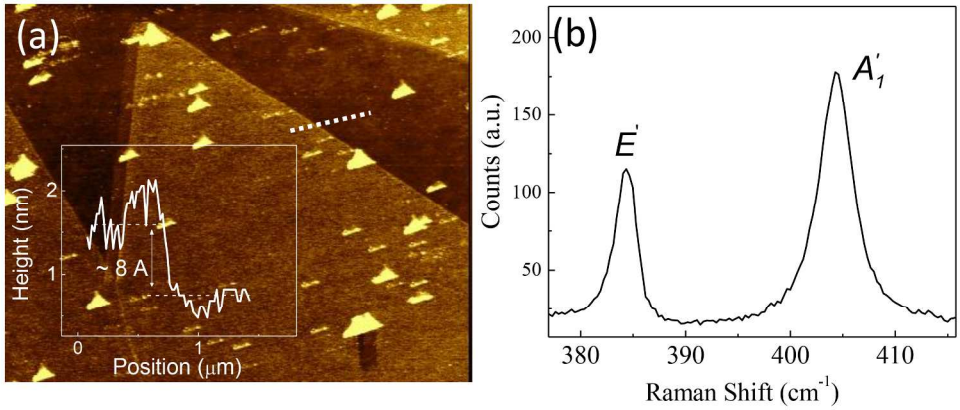

Figure S2: (a) AFM image of a CVD grown sample. The height profile along the black dash is shown in the inset. (b) Raman spectroscopy of a CVD sample.

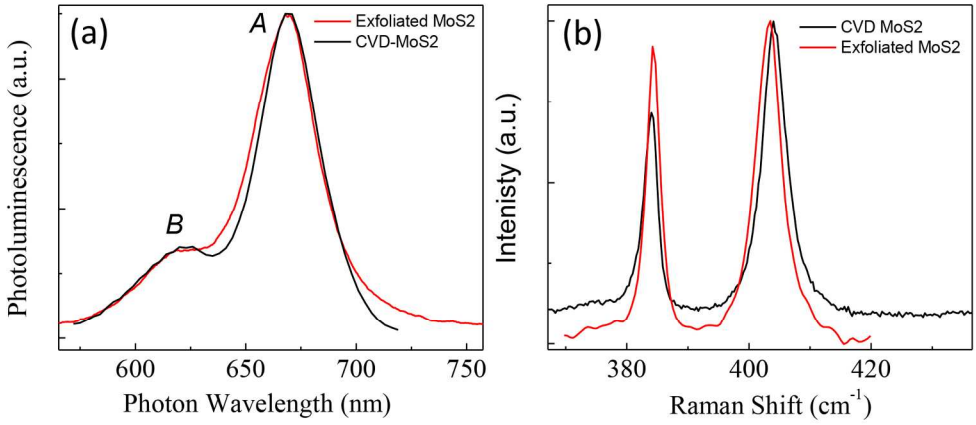

Figure S3: (a) A direct comparison of PL spectrum from CVD grown sample (black) and micro-exfoliated sample (red). (b) Comparison of Raman data for CVD sample and micro-exfoliated sample.

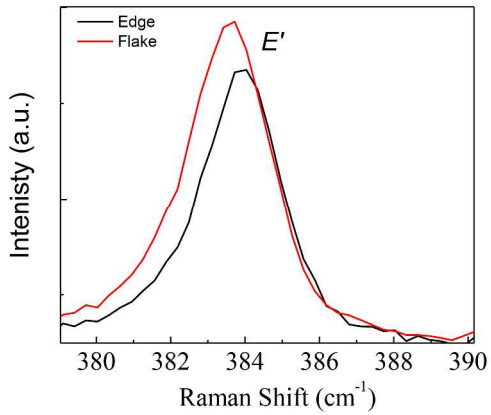

Figure S4: The Raman spectrum of CVD sample obtained from the edges (black line) and from the middle of the flake (red line).

S3: Blue shift of the *A*-peak and the edge fluorescent brightness

Figure S5 presents the blue shift of the *A*-exciton peak and fluorescence brightness of the edges compared to middle of the flake for all the samples.

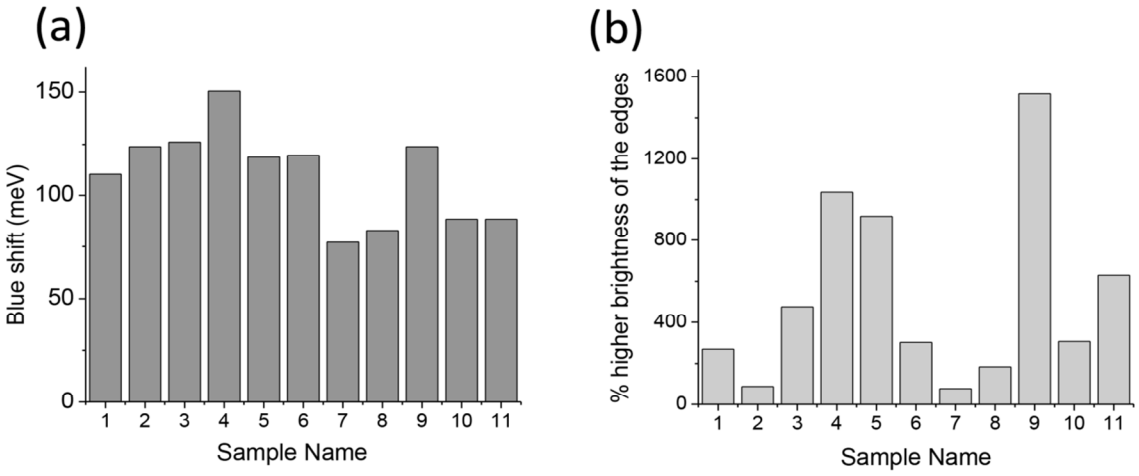

Figure S5: (a) The measured blue shift of the *A*-exciton peak for the PL from the edges of different samples when compared to the point inside. (b) Plot for the luminescence brightness of the outermost edges when compared to the luminescence from the point inside.

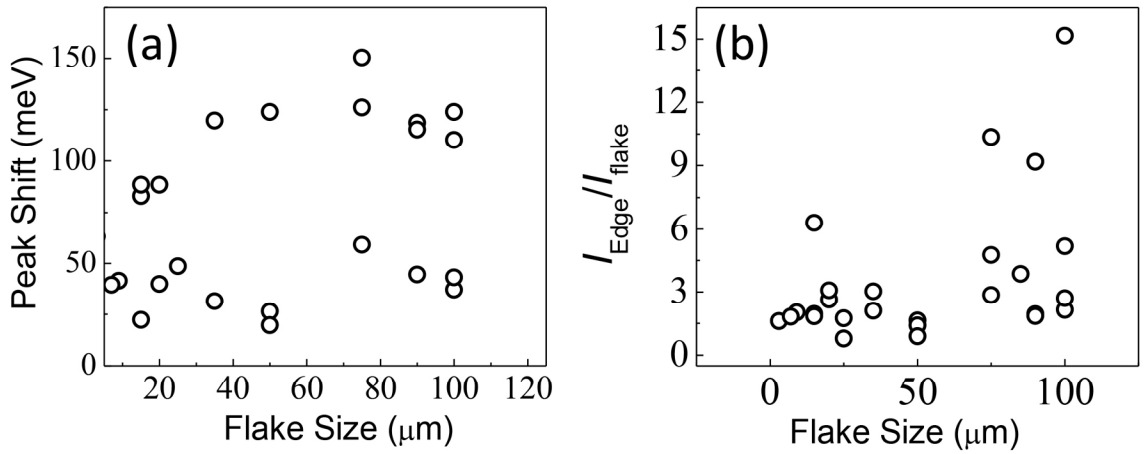

FigureS6: (a) Peak shift as a function of flake sizes and (b) the ratio of PI intensity from the edges to the middle of the flake as a function of flake sizes.

S4: Experimental determination of the beam diameter

We have used fluorescent microspheres beads of size 200nm (Thermofisher, Catalog No-T14792). The fluorescence image of such beads is shown in Figure S7. Here the excitation laser wavelength is 405nm.

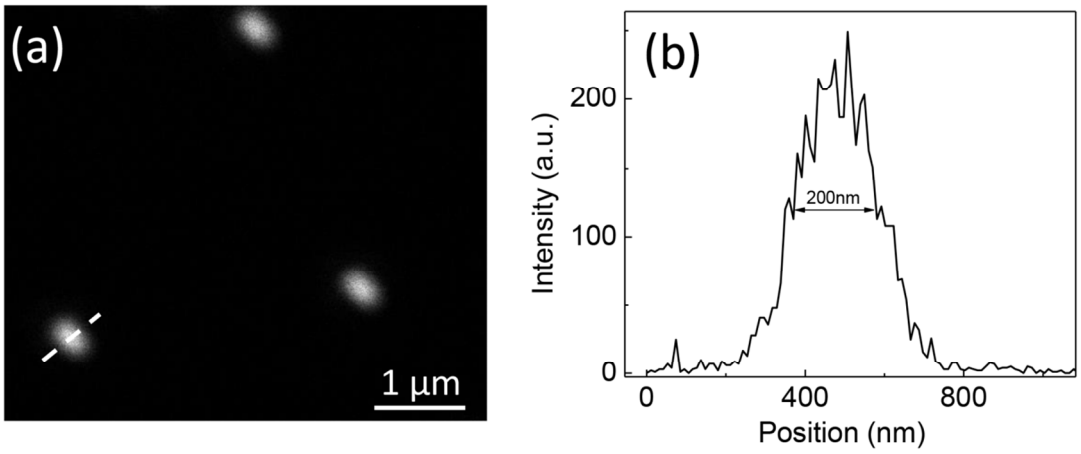

Figure S7: (a) Fluorescence image of microsphere beads. The scale bar is 1 micron. (b) The intensity plot along the white dashed line shown in figure (a).

S5: Calculation of Local electrostatic potential and charge distribution

Fig.S8 shows the calculated electrostatic potential along the ribbon. The asymmetric potential, which is lower at the Mo-edge, where the oxygen dimer adsorbed, and lifted at the S-edge, as compared to the symmetric curve of the pristine MoS_2 ribbon, is caused by the oxygen atoms. The downshifted local electrostatic potential agrees with the lower valence band position close to the Mo-edge (Figure 4 in the main text). We believe that the excess electrons at the Mo-edge and the oxygen atoms cause a surface dipole pointing towards the nanoribbon leading to the lower local electrostatic potential, or correspondingly a higher local work function.

Moreover, Bader charge[1] in Fig. S8 (bottom panel) shows that the Mo atoms at the Mo-edge have less electrons when an oxygen dimer replaces an S atom. It should be noted that Mo has 6 valence electrons. The Bader charge suggests that most Mo atoms are Mo^{2+}, and oxygen further withdraws electrons due to its higher electronegativity leading to a higher oxidation state of the Mo atom at the Mo-edge. The metallic nature of the Mo-edge and the excess electrons at the oxygen helps to screen the Coulombic interaction in the exciton.

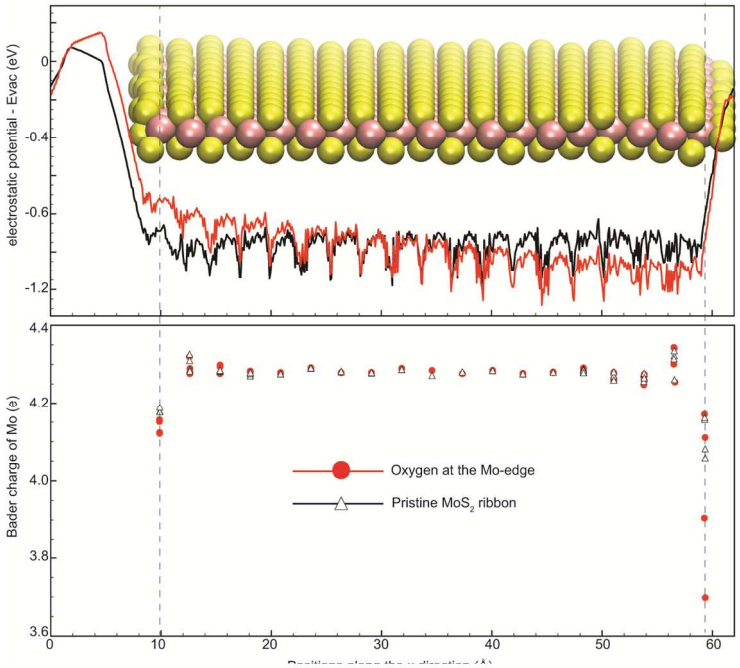

Figure S8: Calculated local electrostatic potential and Bader charge distribution with (red) and without (black) oxygen at the Mo-edge of the MoS_2 nanoribbon. (top) The averaged electrostatic potential of the *y*-plane, (perpendicular to the paper) and along the infinite ribbon direction, plotted as a function of the position along the *x*-direction. Vacuum level is set to zero. (bottom) the Bader charge plotted as a function of the *x* coordinate of each Mo atom. The two dashed lines indicate the edge positions.

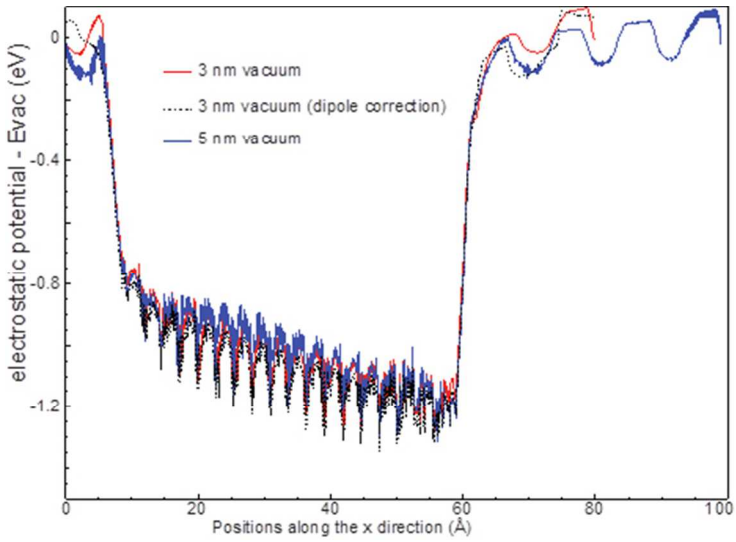

Fig.S9: Calculated electrostatic potential along the ribbon (the same as Fig. S8) with different thickness of vacuum layer (3nm (red solid) and 5nm (blue solid)) inserted between the adjacent ribbons along the ribbon direction. Dipole correction has also been used to converge the potential, and the result is shown to compare (black dashed).

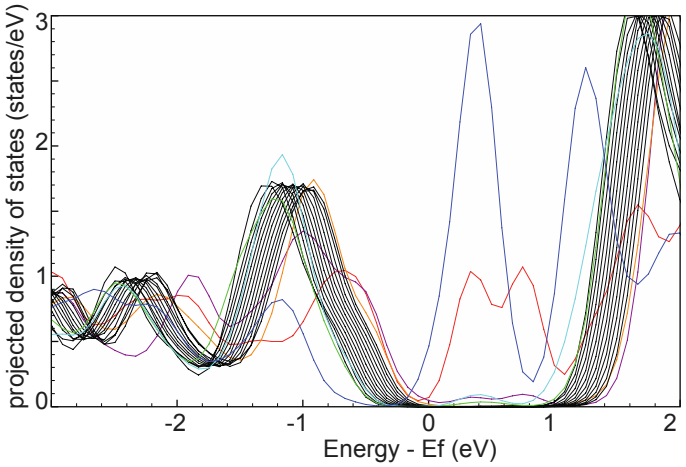

Figure S10: Projected DOS onto Mo atoms along the ribbon with the S vacancy at the Mo-edge occupied by one O atom.

References:

1. Henkelman, G.; Arnaldsson, A.; Jónsson, H., A Fast and Robust Algorithm for Bader Decomposition of Charge Density. *Computational Materials Science* **2006**, *36*, 354-360.